(Received 17 March 2025, Accepted 14 May 2025, Scheduled 27 May 2025)

Sensorless Control Strategy for PMSM Based on Model Reference Adaptive Control Combined with Fast Super-Twisting Algorithm

Feng Yu, Xiping Liu, Zhangqi Liu*, Qiang Ge, and Yuxin Liu

School of Electrical Engineering and Automation, Jiangxi University of Science and Technology, Ganzhou 341000, China

ABSTRACT: To address the issues of large speed fluctuations and slow current convergence in traditional model reference adaptive system (MRAS) algorithms, this paper proposes an improved model reference adaptive algorithm based on the fast super-twisting algorithm (FASTA). First, a feedforward compensation term is introduced into the traditional MRAS framework. Additionally, an adaptive feedback gain coefficient is designed, which can be dynamically adjusted in real-time to track speed variations and adapt to different external operating conditions, thereby effectively reducing speed fluctuation amplitude. Furthermore, a fast super-twisting algorithm with a dynamic adjustment exponential gain term is designed and integrated with the model reference adaptive system, replacing the traditional PI controller used in MRAS, significantly improving convergence speed of the system. Finally, experimental results verify the effectiveness and feasibility of the proposed strategy.

1. INTRODUCTION

Permanent Magnet Synchronous Motors (PMSMs) are widely used in various fields such as household appliances, aerospace, maritime, and new energy vehicles due to their high efficiency, strong coupling, and stable operation [1–4]. Traditional PMSM control requires the installation of position sensors to obtain precise rotor position and speed information, which not only increases the motor's size and cost but also makes PMSM systems prone to sensor failures under harsh operating conditions such as vibration and high humidity [5]. Consequently, sensorless control methods for PMSMs have become a research hotspot in the field of PMSM control.

Currently, the sensorless control of Permanent Magnet Synchronous Motors can be categorized into two types. The first type focuses on zero-speed or ultra-low-speed sensorless control methods, such as low-frequency signal injection [6] and high-frequency signal injection [7]. The second type targets medium-to-high-speed sensorless control methods, including flux observers [8], sliding mode observers (SMOs) [9], Extended Kalman Filter (EKF) [10], Model Reference Adaptive System [11], and artificial intelligence algorithms [12]. Among them, MRAS is widely used for sensorless control of PMSMs in medium-to-high-speed scenarios due to its simplicity of implementation and high accuracy. However, its slow convergence speed and weak anti-interference capability negatively impact the system's control precision and stability [13].

In [14], a fuzzy adaptive rate MRAS speed observation method was proposed, which used current error as the fuzzy control input to improve current utilization. This method addresses speed fluctuations of MRAS under external operational condition changes, but its control law overly relies on model parameters, resulting in weak practicality. In [15], an MRAS method with fuzzy control was introduced to replace traditional proportional-integral (PI) adaptive mechanisms, addressing issues such as insufficient robustness in conventional PI controllers. However, the model complexity reduces its reliability. In [16], a PI controller combined with neural networks and MRAS was proposed, effectively reducing speed control fluctuations, but it heavily depended on motor parameters. In [17], an MRAS incorporating rotor flux was proposed by establishing a voltage compensation model in the system, which eliminated rotor flux errors and enhanced MRAS stability. However, the experiments did not analyze system stability under low-speed conditions. In [18], a second-order sliding mode algorithm was integrated with MRAS, and parameter identification was introduced in the observer, improving anti-interference and chattering suppression capabilities, albeit at the cost of reduced convergence speed. In [19], a combination of SMO and MRAS was implemented using a partitioned sliding mode algorithm, enhancing system convergence speed in high-speed ranges. However, first-order sliding modes induced significant chattering. In [20], an MRAS with current compensation was proposed, compensating speed errors through fundamental and harmonic current vectors to resolve speed fluctuations under current disturbances. However, the system exhibited slow current convergence. In [21], a second-order sliding mode algorithm was combined with MRAS, and stator resistance parameter identification was introduced to address speed errors under parameter mismatches. Experimental results demonstrated that higher-order sliding mode algorithms effectively suppressed chattering caused by MRAS, but the second-order algorithm re-

* Corresponding author: Zhangqi Liu (liuzhq@jxust.edu.cn).

duced system convergence speed. In [22], the chattering mechanism induced by sliding mode control was fundamentally analyzed, and the chattering suppression and dynamic response capabilities of Full-Order Sliding Mode Observer (FO-SMO) and Super-Twisting Sliding Mode MRAS (STM-MRAS) were compared. While the STM algorithm addressed MRAS's insufficient anti-interference capability under constant speeds, it failed to effectively suppress abrupt step disturbances.

To address these challenges, this paper proposes an MRAS observer based on fast super-twisting algorithm and feedforward compensation (FASTA-FC-MRAS), aiming to reduce speed chattering and improve current convergence speed. The academic contributions of this research are summarized as follows:

1) Feedforward compensation is introduced based on the traditional MRAS, and an adaptive feedback gain algorithm is designed to enhance chattering suppression capability.
2) A fast super-twisting algorithm is designed, incorporating a dynamically adjustable exponential gain term in its proportional component to improve current convergence speed.
3) The fast super-twisting algorithm is combined with MRAS theory to enhance the overall dynamic response and static performance of the system.

2. MATHEMATICAL MODEL AND TRADITIONAL MRAS DESIGN

To facilitate the description of the proposed control method, this section presents the mathematical model of the motor and constructs a model reference adaptive system based on the motor model.

2.1. The Mathematical Model of PMSM

The voltage equations of the surface-mounted permanent magnet synchronous motor in the rotating d-q reference frame can be expressed as:

$$\begin{cases} u_d = Ri_d + L_s p i_d - \omega_e \varphi_q \\ u_q = Ri_q + \omega_e \phi_d + L_s p i_q \end{cases} \tag{1}$$

where p denotes the differential operator, and the stator flux linkage equations are expressed as:

$$\begin{cases} \varphi_d = L_s i_d + \varphi_f \\ \varphi_q = L_s i_q \end{cases} \tag{2}$$

For the Surface-Mounted PMSM (SPMSM), $L_s = L_d = L_q$, to simplify, substituting Eq. (2) into (1) yields the following current equation:

$$\begin{cases} p i_d = -\frac{R}{L_s} i_d + \omega_e i_q + \frac{u_d}{L_s} \\ p i_q = -\frac{R}{L_s} i_q - \omega_e i_d - \frac{\varphi_f}{L_s}\omega_e + \frac{u_q}{L_s} \end{cases} \tag{3}$$

where i_d and i_q represent the d-axis and q-axis stator currents, respectively; u_d and u_q represent the d-axis and q-axis stator voltages; R and L_s represent the stator resistance and inductance, respectively; ω_e denotes the electrical angular velocity of the motor; and φ_f represents the rotor permanent magnet flux linkage.

2.2. Conventional MRAS

The conventional MRAS method does not integrate the equations of the unknown variables as a reference model, but uses the stator equation as an adjustable model to estimate the variable parameters. The adjustable model is adjusted by monitoring the d-axis and q-axis stator currents i_d and i_q of the motor and comparing them with the reference model. The current mathematical model shown in Eq. (3) is constructed by including the speed estimation required for the adjustable model. The current error is adjusted by a PI controller to obtain rotor position of the motor and speed estimation. The expression for the reference model is given below:

$$p\begin{bmatrix} i_d' \\ i_q' \end{bmatrix} = \begin{bmatrix} \frac{-R}{L_s} & \omega_e \\ -\omega_e & \frac{-R}{L_s} \end{bmatrix}\begin{bmatrix} i_d' \\ i_q' \end{bmatrix} - \frac{1}{L_s}\begin{bmatrix} u_d' \\ u_q' \end{bmatrix} \tag{4}$$

where:

$$\begin{cases} i_d' = i_d + \frac{\varphi_f}{L_s} \\ i_q' = i_q \\ u_d' = u_d + \frac{R\varphi_f}{L_s} \\ u_q' = u_q \end{cases} \tag{5}$$

where the prime symbol " ′ " is used for convenience in the subsequent derivation, and the model also contains parameters that need to be recognized by the reference frame.

By substituting the measured currents and speed in Eq. (4) with the estimated current and speed values, an MRAS adjustable model containing rotor information can be obtained.

$$p\begin{bmatrix} \hat{i}_d' \\ \hat{i}_q' \end{bmatrix} = \begin{bmatrix} \frac{-R}{L_s} & \hat{\omega}_e \\ -\hat{\omega}_e & \frac{-R}{L_s} \end{bmatrix}\begin{bmatrix} \hat{i}_d' \\ \hat{i}_q' \end{bmatrix} - \frac{1}{L_s}\begin{bmatrix} u_d' \\ u_q' \end{bmatrix} \tag{6}$$

In the equations, "∧" denotes the estimated value of the corresponding parameter.

As illustrated in Figure 1, the reference model provides the actual stator currents values, whereas the adjustable model generates their estimated counterparts. The stator current error dynamics equation is derived by subtracting Eq. (4) from Eq. (6),

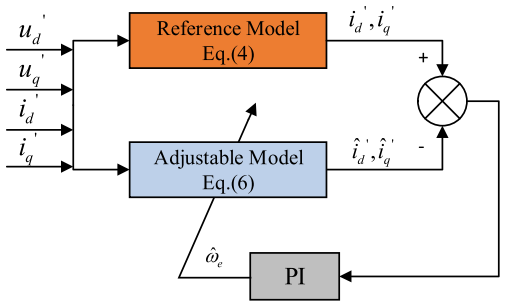

FIGURE 1. Block diagram of the conventional MRAS.

expressed as:

$$p\begin{bmatrix}\tilde{i}_d\\ \tilde{i}_q\end{bmatrix} = A\begin{bmatrix}\tilde{i}_d\\ \tilde{i}_q\end{bmatrix} - J(\omega_e-\hat{\omega}_e)\begin{bmatrix}\hat{i}_d'\\ \hat{i}_q'\end{bmatrix} \tag{7}$$

where:

$$\tilde{i}_d = i_d' - \hat{i}_d', \quad \tilde{i}_q = i_q' - \hat{i}_q',$$
$$A = \begin{bmatrix}-\frac{R}{L_s} & \omega_e\\ -\omega_e & -\frac{R}{L_s}\end{bmatrix}, \ J = \begin{bmatrix}0 & -1\\ 1 & 0\end{bmatrix} \tag{8}$$

In the equation, $\hat{i}_d$ and $\hat{i}_q$ represent the estimated current errors of i_d and i_q, respectively. In accordance with Popov's hyperstability theory [23], the estimated speed derived from the conventional MRAS speed estimation method can be expressed as:

$$\hat{\omega}_e = \left(k_p + \frac{k_i}{s}\right)\left(i_d\hat{i}_q - \hat{i}_d i_q - \frac{\varphi_f}{L_s}(i_d - \hat{i}_q)\right) \tag{9}$$

The adaptive mechanism represented by Eq. (9) can be regarded as a PI controller, where K_p and K_i are the proportional and integral coefficients of the PI controller, respectively, and $1/s$ denotes the integral operator symbol. In the PI controller, K_p determines the response speed of the model, but excessive sensitivity will lead to model overshoot. When the error between the reference model and adjustable model converges to zero, the estimated motor speed approaches the actual speed. Additionally, as seen from Eq. (19) and Figure 1, the estimated motor speed serves as an adjustable parameter of the adjustable model. In MRAS-based speed estimation, by comparing the outputs of the reference model (Eq. (4)) and the adjustable model (Eq. (6)), and utilizing a PI controller to tune the parameters of the adjustable model, the output of the adjustable model gradually converges to that of the reference model, thereby achieving accurate estimation of the actual motor speed.

3. THE DESIGN OF FASTA-FC-MRAS

3.1. MRAS Design with Feedforward Compensation

In conventional MRAS, the system relies on the error between the reference model and adjustable model, and the error is gradually adjusted through a PI controller to make the estimated speed progressively approach the actual speed. However, this closed-loop adjustment method has certain limitations because the error correction depends on the accumulation of time and the feedback process, which results in a delayed system response and is difficult to keep up with the actual changes, potentially leading to a gradual increase in the error. To improve the convergence speed between the reference model and adjustable model, a feedforward compensation mechanism is introduced. Adjusting the output of the adjustable model through feedforward compensation accelerates the error convergence process between the models and improves the response speed of the system. The structure of the feedback correction MRAS is shown in Figure 2.

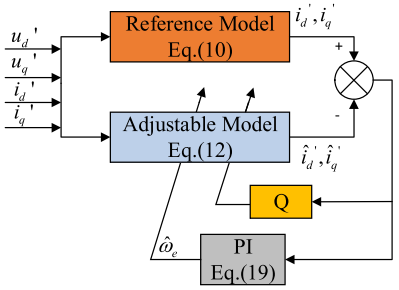

FIGURE 2. Block diagram of the MRAS incorporating feedforward compensation.

The adjustable model can be derived from the following equations:

$$p\begin{bmatrix}i_d'\\ i_q'\end{bmatrix} = A\begin{bmatrix}i_d'\\ i_q'\end{bmatrix} + B\begin{bmatrix}u_d'\\ u_q'\end{bmatrix} + C \tag{10}$$

where:

$$A = \begin{bmatrix}-\frac{R}{L_s} & \omega_r\\ -\omega_r & -\frac{R}{L_s}\end{bmatrix}, \ B = \begin{bmatrix}\frac{1}{L_s} & 0\\ 0 & \frac{1}{L_s}\end{bmatrix},$$
$$C = \begin{bmatrix}0\\ -\frac{\varphi_f}{L_s}\omega_f\end{bmatrix} \tag{11}$$

By replacing the corresponding variables in Eq. (1) with their estimated values and incorporating the feedforward compensation mechanism, the adjustable model expressed by the state observer equation can be obtained as:

$$p\begin{bmatrix}\hat{i}_d'\\ \hat{i}_q'\end{bmatrix} = \hat{A}\begin{bmatrix}\hat{i}_d\\ \hat{i}_q\end{bmatrix} + B\begin{bmatrix}u_d\\ u_q\end{bmatrix} + \hat{C} + Q\begin{bmatrix}i_d' - \hat{i}_d'\\ i_q' - \hat{i}_q'\end{bmatrix} \tag{12}$$

where:

$$\hat{A} = \begin{bmatrix}-\frac{R}{L_s} & \hat{\omega}_r\\ -\hat{\omega}_r & -\frac{R}{L_s}\end{bmatrix}, \ B = \begin{bmatrix}\frac{1}{L_s} & 0\\ 0 & \frac{1}{L_s}\end{bmatrix},$$
$$\hat{C} = \begin{bmatrix}0\\ -\frac{\varphi_f}{L_s}\hat{\omega}_r\end{bmatrix} \tag{13}$$

As shown in Figure 2 and Eq. (10), $Q(i_s - \hat{i}_s)$ is the feedforward compensation function, and Q is the feedforward compensation gain matrix. The selection of Q must satisfy the stability requirements of the observer. By subtracting Eq. (10) from Eq. (12), Eq. (14) can be obtained.

$$p\begin{bmatrix}\tilde{i}_d'\\ \tilde{i}_q'\end{bmatrix} = (A+Q)\begin{bmatrix}\tilde{i}_d'\\ \tilde{i}_q'\end{bmatrix} - J(\omega_r - \hat{\omega}_r)\begin{bmatrix}\hat{i}_d'\\ \hat{i}_q'\end{bmatrix}$$
$$-\frac{\varphi_f}{L_s}\begin{bmatrix}0\\ \omega_r - \hat{\omega}_r\end{bmatrix} \tag{14}$$

According to the hyper-stability theory of Popov, while satisfying the observer stability requirements, the feedforward compensation gain matrix Q is selected based on the pole placement principle as follows:

$$Q = \begin{bmatrix} -G_1 & G_2 \\ -G_2 & -G_1 \end{bmatrix} \tag{15}$$

Furthermore, the following conditions must be satisfied by G_1 and G_2:

$$\begin{cases} G_1 = (\eta + 1)\frac{R}{L_s} \\ G_2 = (\eta + 1)\hat{\omega}_r \end{cases} \tag{16}$$

where η is a to-be-designed constant satisfying $\eta > 1$.

Expanding Eq. (12) yields the following expression:

$$p\begin{bmatrix} \tilde{i}_d' \\ \tilde{i}_q' \end{bmatrix} = \begin{bmatrix} -(\eta+2)\frac{R}{L_s} & (\eta+2)\hat{\omega}_e \\ -(\eta+2)\hat{\omega}_e & -(\eta+2)\frac{R}{L_s} \end{bmatrix}\begin{bmatrix} \tilde{i}_d' \\ \tilde{i}_q' \end{bmatrix} - \begin{bmatrix} 0 & \omega_e - \hat{\omega}_e \\ -(\omega_e - \hat{\omega}_e) & 0 \end{bmatrix}\begin{bmatrix} \hat{i}_d' \\ \hat{i}_q' \end{bmatrix} \tag{17}$$

From Eq. (13), it can be seen that the diagonal elements of the matrix are all negative, which satisfies the stability condition. Further analysis of the difference between the matrices A in Eq. (7) and $A + Q$ in Eq. (14) reveals that, compared to the traditional MRAS, the MRAS with feedforward compensation introduces a feedforward correction term into the model structure, effectively forming a closed-loop state estimation and significantly accelerating the error convergence process between the adjustable model and reference model. In this way, feedforward compensation not only improves convergence speed of the model but also effectively reduces sensitivity of the system to model uncertainties, thereby enhancing the overall stability and robustness of the system. To avoid oscillations caused by excessive feedforward gain, the design of the feedforward gain coefficient must follow certain guidelines.

The mathematical expression for the estimated speed can be expressed as:

$$\hat{\omega}_e = \left(k_p + \frac{k_i}{s}\right)\left(i_d\hat{i}_q - \hat{i}_d i_q - \frac{\varphi_f}{L_s}(i_d - \hat{i}_q)\right) \tag{18}$$

The block diagram of the system is illustrated in Figure 2.

3.2. Design of the FASTA-FC-MRAS

In the traditional MRAS, the robustness of the PI adaptive mechanism is not strong, and in the presence of external disturbances, it is difficult to achieve optimal control. To address this issue, some researchers have proposed first-order sliding mode control, utilizing the inherent strong robustness of sliding mode to enhance anti-interference capability of the system. However, first-order sliding mode control requires the introduction of a low-pass filter to suppress chattering, which causes phase delay in the system. To solve this problem, the super-twisting algorithm has been introduced as a solution. STA is essentially a second-order sliding mode algorithm that, while providing good robustness, also introduces continuous integral terms to effectively alleviate the chattering phenomenon. Its STA mathematical formulation is as follows:

$$\begin{cases} \dot{x}_1 = -K_1|x_1|^{0.5}\text{sgn}(x_1) + x_2 \\ \dot{x}_2 = -K_2\text{sgn}(x_1) + \rho \end{cases} \tag{19}$$

In the equation, x_1 and x_2 are state variables; $\dot{x}_1$ and $\dot{x}_2$ are the corresponding variable derivatives; K_1 and K_2 are the sliding mode gain coefficients; ρ is the disturbance variable; and sgn is the sign function. The chattering problem in traditional sliding mode control is caused by the sign function. However, STA mitigates the chattering issue significantly by adding continuous integral terms before the sign function and incorporating higher-order derivatives. The sliding mode coefficient satisfies the stability condition as follows:

$$\begin{cases} K_1 > 2\mu_1 \\ K_2 > K_1\frac{5\mu_1 K_1 + 4\mu_1^2}{2(K_1 - 2\mu_1)} \end{cases} \tag{20}$$

The boundary conditions of the disturbance term are satisfied:

$$\begin{cases} \rho_1 \leqslant \mu_1 |x_1|^{1/2} \\ \rho_2 = 0 \end{cases} \tag{21}$$

The equation is as follows: μ_1 is a constant.

To accelerate the sliding mode convergence rate, the Fast Super-Twisting algorithm is introduced, with its FASTA design outlined as follows:

$$\begin{cases} \dot{x}_1 = -K_1|x_1|^{0.5}\text{sgn}(x_1) + x_2 + \gamma_1|x_1|^g x_1 \\ \dot{x}_2 = -K_2\text{sgn}(x_1) + \gamma_2 x_1 + \rho \end{cases} \tag{22}$$

where $\gamma_1|x_1|^g x_1$ denotes the linear smoothing term, γ_1 the speed regulation factor of the smoothing term, and g the adjustment factor for accelerating the sliding mode reaching velocity. The parameter γ_2 is designed to enhance system robustness. The stability of the FASTA algorithm will be formally proven in Proof 1. Moreover, to satisfy the speed performance requirements of motors under various operating conditions, an adaptive gain coefficient control law is proposed in this work. The parameter design criteria are specified as follows:

$$\begin{cases} K_1 = \mu_1\omega^2 \\ K_2 = \mu_2\omega^{3/2} \\ \gamma_1 = \mu_3\omega^3 \\ \gamma_2 = \mu_4\omega^{3/2} \end{cases} \tag{23}$$

where $\mu_i \geq 0, \omega = \omega_e^*/\omega_e$.

To guarantee the stability of the proposed FASTA, the disturbance terms must satisfy the conditions specified in [24].

$$\begin{cases} |\rho_1| \leqslant \lambda_1|\tilde{i}_{dq}|^{1/2} + \lambda_2|\tilde{i}_{dq}| \\ \rho_2 = 0 \end{cases} \tag{24}$$

where $\lambda_i \geq 0$.

When the perturbation term satisfies the above equation, it ensures that the FASTA algorithm is able to stabilize the convergence to the sliding film surface, which leads to the convergence of the system error to zero.

The conditions for sliding mode coefficients are discussed in [25], and these coefficients must satisfy the following requirements:

$$\begin{cases} K_1 > 2\lambda_1 \\ K_2 > \max\left(K_1 \frac{\lambda_1 K_1 + \frac{1}{8}^2\lambda}{2(\frac{1}{2}k_1 - \lambda_1)}, \frac{(\gamma_1\lambda_1 + \frac{1}{2}K_1\lambda_2)^2 + \frac{3}{2}K_1\gamma_1\lambda_1 - 2(\gamma_1 - \frac{1}{4}\lambda_2)K_1^2}{2\gamma_1(\gamma_1 - 2\lambda_2)} \right) \\ \gamma_1 > 2\lambda_2 \\ \gamma_2 > \max\left(\gamma_1 \frac{\left[\gamma_1(\gamma_1 + 3\lambda_2) + \frac{1}{2}\lambda_2^2\right]}{\gamma_1 - 2\lambda_2}, \frac{K_1\left[\frac{1}{2}K_1(K_1 + \frac{1}{2}\lambda_1)^2(2\gamma_1^2 - \frac{3}{2}\lambda_2\gamma_1)\right] + K_1\left[\left(\frac{5}{2}\gamma_1^2 + \frac{3}{2}\lambda_2\gamma_1^2\right)p_1\right]}{2\left(p_1 - \frac{1}{2}K_1(K_1 + \frac{1}{2}\lambda_1)^2\right)\left(\frac{1}{2}K_1 - \lambda_1\right)} - \frac{1}{2}\gamma_1^2 \right) \end{cases} \tag{25}$$

where $p_1 \triangleq \frac{1}{4}K_1^3 + \left(\frac{1}{2}K_1 - \lambda_1\right)\left(2K_2 + \frac{1}{2}K_1^2\right)$.

The above K_1, K_1, γ_1, γ_2 conditions are satisfied, which enables the FASTA algorithm to stabilize and converge in the domain of convergence.

Proof 1: When FASTA is stable and the range of the parameter $|i_{dq}|$ is confined to a small interval, it is guaranteed that a sufficiently large constant M_i can be chosen as follows:

$$\lambda = \begin{pmatrix} \lambda_1 \\ \lambda_1 \end{pmatrix} = \begin{pmatrix} M_1 \\ M_2 \end{pmatrix} \omega^{3/2} \tag{26}$$

Substituting Eq. (21) into (19) yields:

$$\begin{cases} |\rho_1| \leq M_1\omega^{3/2}|i_{dq}|^{1/2} + M_2\omega^{3/2}|i_{dq}| \\ \rho_2 = 0 \end{cases} \tag{27}$$

Therefore, there exists a sufficiently large number μ_1 and μ_2 that ensure the stability of K_1 and K_2.

$$\begin{cases} K_1 = \mu_1\omega^2 > M_1 = M_1\omega^2 + 3M_2\omega^{3/2} \\ K_2 = \mu_2\omega^{3/2} > M_2 = 2M_1\omega^{3/2} + 5M_2\omega^{3/2} \end{cases} \tag{28}$$

Substituting $K_1 = \mu_1\omega^2$, $K_2 = \mu_2\omega^{3/2}$ into $\lambda_1 = M_1\omega^{3/2}$ and $\lambda_2 = M_2\omega^{3/2}$ yields the stability of K_1 and K_2.

$$K_2 = \mu_2\omega^{3/2} > \text{MAX}\left(Q\omega^{3/2}, Q\omega^{3/2}\right) \tag{29}$$

where

$$\begin{aligned} Q_1 &= \frac{\lambda_1\left(M_1\mu_1 + \frac{1}{8}M_1^2\right)}{\mu_1 - 2M_1} \\ Q_2 &= \frac{\left(\mu_2 M_1 + \frac{1}{2}\mu_1 M_2\right)^2}{2\mu_2(\mu_2 - 2M_2)} \end{aligned} \tag{30}$$

Similarly, substituting $K_1 = \mu_1\omega^2$, $K_2 = \mu_2\omega^{3/2}$, $\gamma_1 = \mu_3\omega^3$ and $\gamma_2 = \mu_4\omega^{3/2}$ into $\lambda_1 = M_1\omega^{3/2}$ and $\lambda_2 = M_2\omega^{3/2}$ yields the stability conditions for γ_1 and γ_2:

$$\gamma_1 = \mu_2\omega^3 > \text{MAX}\left(Q_3\omega^3, Q_4\omega^3\right) \tag{31}$$

where

$$\begin{cases} Q_3 = \frac{\mu_1\left(\frac{1}{2}\mu_1\left(\mu_1 + \frac{1}{2}M_1\right)^2\left(2\mu_3^2 - \frac{3}{2}\mu_3 M_2\right)\right)}{2\left(\frac{1}{2}\mu_1 - M_1\right)\left(Q_5 - \frac{1}{2}\mu_1\left(\mu_1 + \frac{1}{2}M_1\right)^2\right)} \\ Q_4 = \frac{\mu_1 Q_5\left(\frac{5}{2}\mu_3^2 + \frac{3}{2}M_2\mu_3\right)}{2\left(\frac{1}{2}\mu_1 - M_1\right)\left(Q_5 - \frac{1}{2}\mu_1\left(\mu_1 + \frac{1}{2}M_1\right)^2\right)} - \frac{1}{2}\mu_3^2 \\ Q_5 = \frac{1}{2}\mu_1^3 + \mu_1\mu_2 - 2\mu_2 M_1 - \frac{1}{2}\mu_1^2 M_1 \end{cases} \tag{32}$$

For given parameters μ_1, μ_2, μ_3, M_1, and M_2, such that μ_4 satisfies:

$$\gamma_2 = \mu_4\omega^{3/2} > \text{MAX}\left(Q_3\omega^{3/2}, Q_4\omega^{3/2}\right) \tag{33}$$

Based on the aforementioned analysis, the adaptive algorithm proposed in the literature is coupled with the motor speed while ensuring system stability. This method effectively suppresses chattering across the entire speed range under varying operating conditions.

The schematic diagram of the adaptive fast super-twisting algorithm is shown in Figure 3.

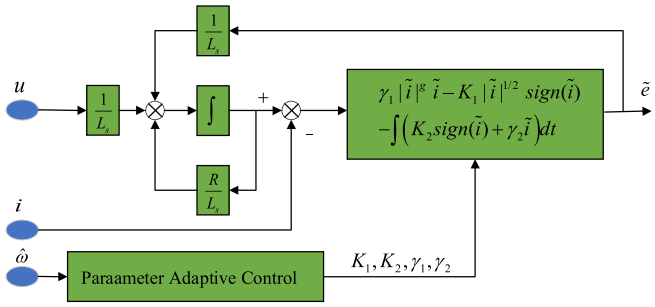

FIGURE 3. FASTA algorithm schematic.

Based on the adaptive mechanism in Eq. (19), a sliding surface is constructed on the error between the reference model and adjustable model.

$$s = e = \left(i_d\hat{i}_q - \hat{i}_d i_q - \frac{\varphi_f}{L_s}(i_q - \hat{i}_q)\right) \tag{34}$$

By incorporating the mathematical model of the PMSM, differentiating Eq. (35) yields:

$$\begin{aligned} \dot{s} &= \dot{e} = i_d i_q + i_d i_q - i_d i_q - \frac{\varphi_f\left(\dot{i}_q - \dot{\hat{i}}_q\right)}{L_s} \\ &= (\omega_r - \hat{\omega}_r)\left(i_d i_q + i_d i_q + \frac{\varphi_f}{L_s}\left(i_d + \hat{i}_q\right) + \left(\frac{\varphi_f}{L_s}\right)^2\right) \\ &\quad + \left(2\frac{R}{L_s}\left(\hat{i}_d i_q - i_d\hat{i}_q\right) + \frac{u_q}{L_s}\left(i_d - \hat{i}_d\right)\left(\frac{R\varphi_f}{L_s^2} - \frac{u_d}{L_s}\right)\right. \\ &\quad \left.\left(i_q - \hat{i}_q\right)\right) \end{aligned} \tag{35}$$

As demonstrated in Eq. (36), when the system state reaches the sliding mode $s = \dot{s} = 0$, the output error between the reference model and adjustable model vanishes, and the rotor speed estimated by MRAS converges to the actual value.

Combining the sliding mode surface and Eq. (3), the adaptive mechanism based on FC-MRAS can be expressed as:

$$\hat{\omega}_e = K_1|\tilde{s}|^{0.5}\mathrm{sgn}(\tilde{s}) + \int_0^t (K_2\mathrm{sgn}(\tilde{s}) + \gamma_2\tilde{s})\,dt + \gamma_1|\tilde{s}|^g s \quad (36)$$

The estimated rotor position can be obtained by integrating the estimated motor speed.

$$\hat{\theta} = \int_0^t \hat{\omega}_r dt \quad (37)$$

3.3. Improved Piecewise Saturation Function

In essence, using a discontinuous switching sign function causes significant chattering. While adding a low-pass filter can reduce chattering, it also introduces phase lag issues. Therefore, replacing the sign function and eliminating the use of the lowpass filter (LPF) are key to solving this problem. To reduce the chattering caused by the switching function, a buffer zone is added to the switching function. Here, a smooth Sigmoid sine-type saturation function will be used.

The expression for the piecewise sine-type saturation function is:

$$S_d(x) = \begin{cases} -1 & x \le c \\ \frac{2}{1+e^{-ux}} - 1 & c < x < c \\ 1 & x \ge c \end{cases} \quad (38)$$

Combining (38) and (40), we obtain:

$$\hat{\omega}_e = K_1|\tilde{s}|^{0.5}S_d(\tilde{s}) + \int_0^t (S_d(\tilde{s}) + \gamma_1\tilde{s})dt + \gamma_2|\tilde{s}|^g\tilde{s} \quad (39)$$

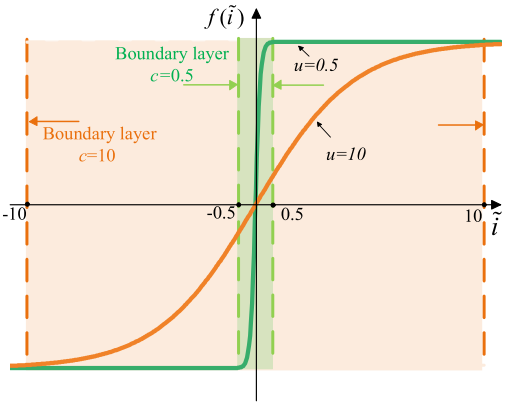

FIGURE 4. The curve of the improved sigmoid function.

According to the analysis of literature [25] and Figure 4, it can be concluded that the Sigmoid sine-type saturation function is smooth and continuous in the real number domain, and it is linear at the zero-point position, effectively suppressing chattering. The parameter u is used to adjust the slope near the zero-point position: the larger the value is, the more oscillatory the curve becomes, making it resemble the sign function. The boundary factor c controls the thickness of the boundary layer. The Sigmoid function is used within the boundary layer, while the sign function is used outside the boundary layer. A larger boundary layer improves chattering suppression but slows down the dynamic response, whereas a smaller boundary layer increases dynamic response speed but reduces chattering suppression. Therefore, selecting appropriate values for u and c is crucial for balancing control accuracy and dynamic response speed in the system.

The schematic diagram of the improved saturation function-based FASTA-MRAS is shown in Figure 5.

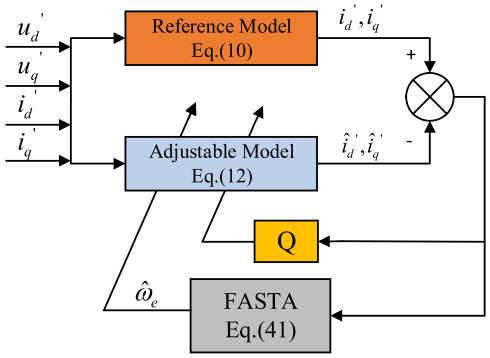

FIGURE 5. Based on the FASTA-FC-MRAS structural diagram.

3.4. Parameter Optimization Design

From the analysis in the previous section, it can be concluded that the parameters η, u, and c have a decisive impact on the chattering suppression characteristics and dynamic response performance of the FASTA algorithm. To obtain the optimal parameter combination, this section conducts comparative experiments to study the effects of different parameter combina-

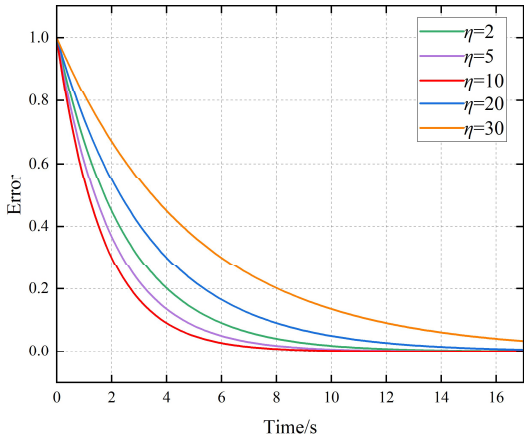

FIGURE 6. Convergence error under different η.

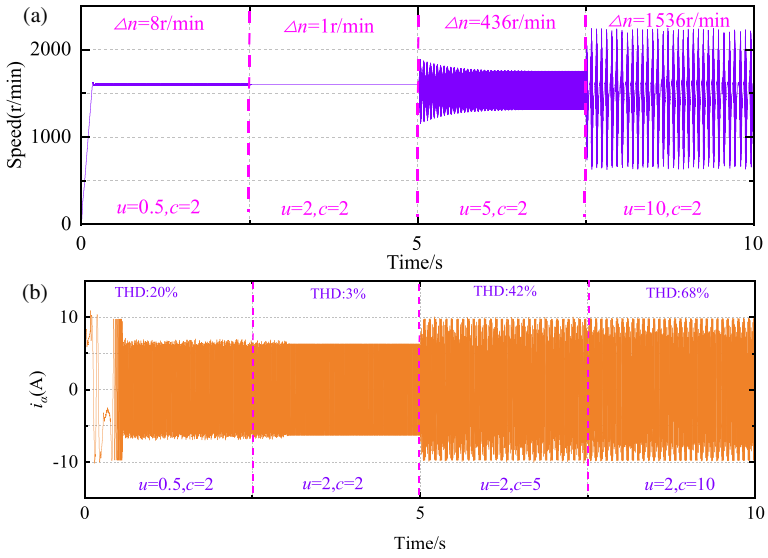

FIGURE 7. The effect of different u and c on speed and current.

tions on the motor speed and i_α current. In this section, comparative experiments will be conducted to investigate the effect of different parameter combinations on the performance of the system.

In control systems, the parameter η has a significant impact on the error convergence and stability of the system. As shown in Figure 6, when $\eta = 2$ or 10, the system response is relatively sluggish, with slower error convergence, and the system may require a longer time to reach a steady state. However, as η increases, the system begins to converge more rapidly, with errors diminishing faster and dynamic responses becoming quicker. Notably, when $\eta = 10$, the system demonstrates optimal convergence speed and stability, indicating that under this ideal η value, the system can rapidly reduce errors while avoiding overshoot and oscillation. Nevertheless, when η continues to increase, the convergence rate begins to slow down, accompanied by a rise in steady-state error. This indicates that excessively large η values may lead to overcompensation, thereby compromising system stability. Therefore, the rational selection of η must strike a balance among error convergence speed, system stability, and response characteristics. Therefore, $\eta = 3$ is an ideal choice of parameter to ensure fast convergence while keeping the system stable.

Figure 7(a) shows a comparison of the speed waveforms corresponding to different values of u while keeping $c = 2$ constant. The experimental results indicate that as the value of u increases from 0.5 to 2, 5, and 10, the speed fluctuation amplitude initially decreases and then increases, showing a nonlinear trend. When $u = 2$, the minimum speed fluctuation is achieved, with $n = 1$ r/min, proving that this parameter effectively suppresses the chattering caused by discontinuous switching functions. It is noteworthy that when u exceeds the critical value of 5, significant high-frequency chattering occurs.

In Figure 7(b), keeping $u = 2$ constant, comparative experiments are conducted with $c = 0.5$, 2, 5, and 10 to observe the total harmonic distortion (THD) of the current. When $c = 2$, the current THD remains at a minimum of 3%. This indicates that as c continues to increase, the current THD also increases.

In conclusion, when u is too large, the slope becomes smaller; the system responds more slowly; and thus, system oscillations are triggered. When c is too large, the boundary layer becomes thicker, which slows down the dynamic response and leads to current distortion. Using $u = 2$ and $c = 5$ results in better dynamic response for the FASTA-FC-MRAS.

4. EXPERIMENTAL VERIFICATION AND ANALYSIS

The experimental test platform for the PMSM sensorless control algorithm is shown in Figure 8. It primarily consists of the following components: a main control chip STM32G431CBU6, an inverter, a host computer, an oscilloscope, a PMSM, and a magnetic powder brake serving as the load. To validate the effectiveness of the proposed control algorithm, a simulation model of the algorithm was developed in MATLAB/Simulink. The generated code was then deployed to the ARM control board for verification. Real-time monitor-

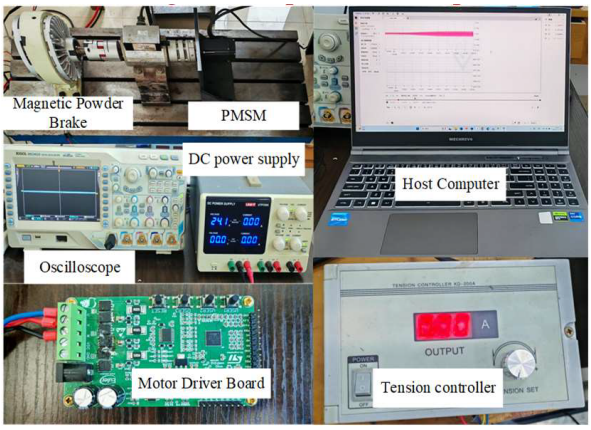

FIGURE 8. Experimental setup of the motor test platform.

TABLE 1. PMSM parameters.

Parameter	Symbol	Values
DC-link voltage	U_{dc}	24 V
Pole Pairs	P_n	5
Stator Resistance	R_s	0.1763 Ω
Stator inductance	L_s	0.195185 mH
Flux linkage	ψ_f	0.0109 Wb
Motion inertia	J	0.001 kg·m^2
Rated speed	ω	2000 r/min

ing of the PMSM operating status was achieved through the oscilloscope.

In this study, the focus lies on investigating the chattering suppression effectiveness and dynamic response speed under different control strategies. Experimental comparisons were conducted among MRAS, STA-MRAS, and FASTA-FC-MRAS to observe motor speed and current under the three control algorithms across various operating conditions. The block diagram of the PMSM sensorless vector control system proposed in this work is illustrated in Figure 9. The PMSM parameters of the experimental platform and the configured experimental settings are detailed in Table 1 and Table 2, respectively.

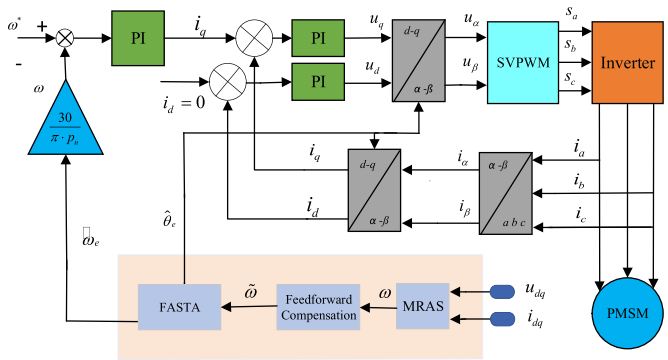

FIGURE 9. FASTA-FC-MRAS-based sensorless control block diagram.

From the analysis in Table 3 regarding the performance of MRAS, STA-MRAS, and FASTA-FC-MRAS in STM32FG431CBU6, although FASTA-FC-MRAS exhibits higher raw computational complexity than MRAS and STA-MRAS, it achieves a 20% reduction in redundant computations through mixed-precision computation.

4.1. Performance Analysis of Rotational Speed Chattering Suppression

Due to the significant speed fluctuations observed with the MRAS control strategy at low speeds, a comprehensive evaluation of its speed performance was conducted. The motor was set to run at a constant speed of 1000 rpm for a period, then increased to 1800 rpm and maintained for a period before being reduced back to 1200 rpm. The speed and current response performance of MRAS, STA-MRAS, and FASTA-FC-MRAS were compared through experiments. The speed variation curves are shown in Figures 10(a), (b), and (c).

TABLE 2. Experimental parameter settings.

Parameter	Values
u	2
c	2
Current PI controller (K_p)	130
Current PI controller (K_i)	290
Speed PI controller (K_p)	0.08
Speed PI controller (K_i)	8
η	10
g	0.5
μ_1	50
μ_2	20
μ_3	150
μ_4	200

As shown in Figure 10(a), the MRAS exhibits pronounced speed fluctuations within the 1200–1800 rpm range, with a speed fluctuation amplitude of 15.5 rpm at 1200 rpm, which decreases to 1200 rpm at 1800 rpm. This result clearly demonstrates the inadequate chattering suppression capability of the MRAS method under low-speed operating conditions.

In Figure 10(b), the STA-MRAS control strategy incorporating the Super-Twisting Algorithm (STA) achieves reduced speed fluctuations of 4.3 rpm at 1200 rpm, further declining to 4.5 rpm at 1800 rpm. Although the continuous integral term in STA enhances chattering suppression and thereby mitigates speed oscillations, residual chattering persists due to the inherent discontinuous switching function.

As illustrated in Figure 10(c), the FASTA-FC-MRAS control strategy, which integrates a Fast Super-Twisting Algorithm, significantly reduces speed fluctuations to approximately 3.5 rpm through an optimized saturation function. This represents a 50% improvement in chattering suppression compared to STA-MRAS. The enhanced strategy markedly diminishes speed oscillations in the model reference adaptive system.

Under a constant speed of 1800 rpm, a 1 Nm load was applied, and the speed fluctuations of MRAS, STA-MRAS, and FASTA-FC-MRAS were observed, as shown in Figures 11(a), (b), and (c), respectively.

After the load increase, the speed of the MRAS system dropped to 1746 rpm, then recovered to the set speed, with a fluctuation amplitude of 11.2 rpm. In contrast, the STA-MRAS system, after the load increase, experienced a speed drop to 1766 rpm and subsequently recovered to the set speed, with a fluctuation amplitude of only 3.8 rpm. Further analysis reveals that the FASTA-FC-MRAS system demonstrates superior dynamic response characteristics during load changes, with a smaller speed drop and a faster stabilization to the set speed, significantly reducing the fluctuation amplitude to 3.6 rpm.

The motor is started under no-load conditions, and the speed fluctuations of MRAS, STA-MRAS, and FASTA-FC-MRAS are observed, as shown in Figures 12(a), (b), and (c), respectively. As shown in Figure 12, the overshoot of MRAS and STA-MRAS are relatively large, at 1826 rpm and 1820 rpm, respectively, and the FASTA-FC-MRAS proposed in this paper exhibits the smallest overshoot during direct startup, reaching a peak speed of 1805 rpm, and the speed fluctuation in the steady-state operation is 3.2 rpm.

TABLE 3. Comparison of embedded implementations of three algorithms.

Control Strategy	Algorithm occupancy (KB)	CPU Utilization (%)	Q15-CPU Utilization (%)
MRAS	36.8 KB	28%	25%
STA-MRAS	41.2 KB	54%	48%
FASTA-FC-MRAS	43.3 KB	72%	52%

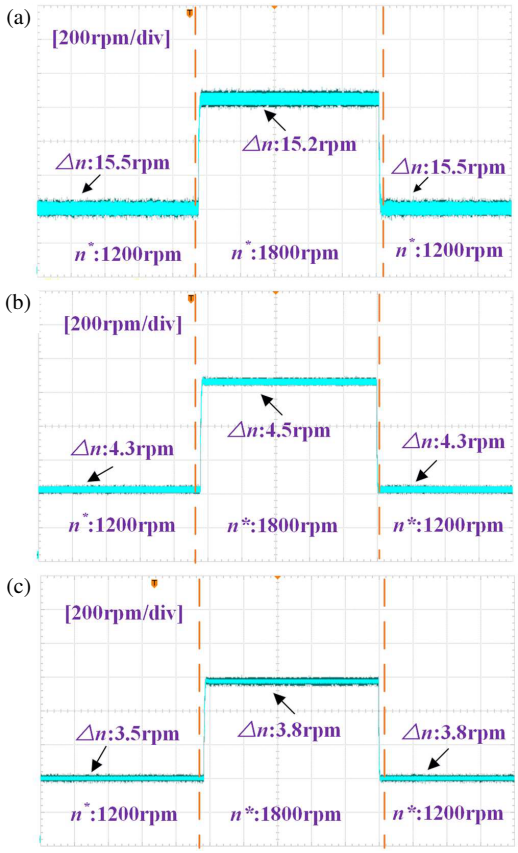

FIGURE 10. Speed variation curve during motor acceleration and deceleration. (a) MRAS, (b) STA-MRAS, (c) FASTA-FC-MRAS.

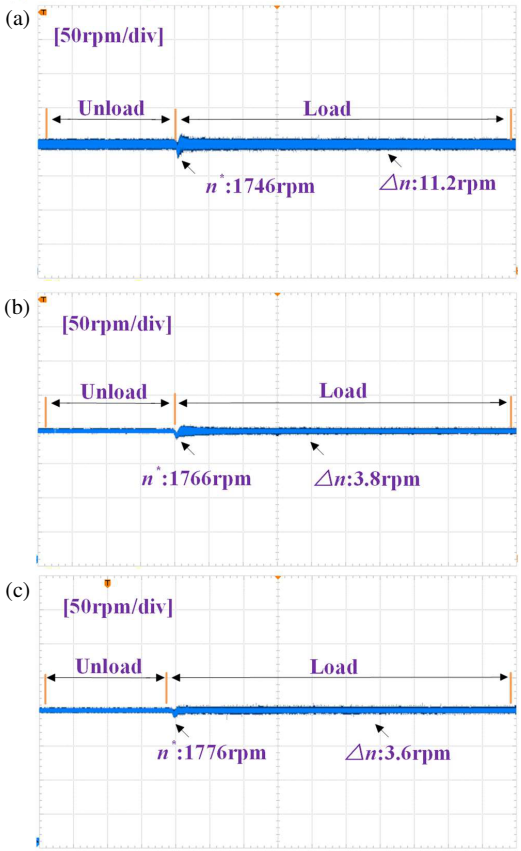

FIGURE 11. Speed curve under load mutation. (a) MRAS, (b) STA-MRAS, (c) FASTA-FC-MRAS.

4.2. Current Stability Analysis

The motor operates at a constant speed of 1200 rpm, and after 2 seconds, a 1 Nm load is applied. The current fluctuations of MRAS, STA-MRAS, and FASTA-FC-MRAS are observed.

As shown in Figure 13, FASTA-FC-MRAS exhibits the lowest harmonic distortion rate, at only 16%. In contrast, MRAS, due to the poor disturbance rejection capability of the PI controller, exhibits the highest distortion rate. Although the current chattering in STA-MRAS is reduced compared to MRAS, its harmonic distortion rate remains high at 25%.

Figure 14 presents the comparison of phase A current under the FC-MRAS and FASTA-FC-MRAS control strategies. It can be observed that the distortion rates of FC-MRAS are higher, reaching 38% when it is unloaded and 26% when it is loaded. With the introduction of the FASTA algorithm, the harmonic distortion rates are reduced to 26% and 13%, respectively.

4.3. Voltage Stability Analysis

To analyze the d-axis voltage of the MRAS, STA-MRAS, and FASTA-FC-MRAS control algorithms, the motor accelerates from 1200 rpm to 1800 rpm, with the experimental results shown in Figures 15(a), (b), (c), (d), (e), and (f).

Figures 15(a), (b), and (c) illustrate that at 1200 rpm, MRAS exhibits the largest voltage fluctuations, with a peak q-axis voltage difference of 0.32 V. At 1800 rpm, the peak q-axis voltage difference decreases to 0.30 V. STA-MRAS shows a peak q-axis voltage difference of 0.32 V at 1200 rpm and 0.28 V at 1800 rpm. In comparison, FASTA-FC-MRAS exhibits smaller voltage fluctuations, with a 59% reduction in voltage fluctuation compared to MRAS and a 56% reduction compared to STA-MRAS.

Furthermore, Figures 15(d), (e), and (f) demonstrate that FASTA-FC-MRAS has a smaller d-axis voltage fluctuation than MRAS and STA-MRAS.

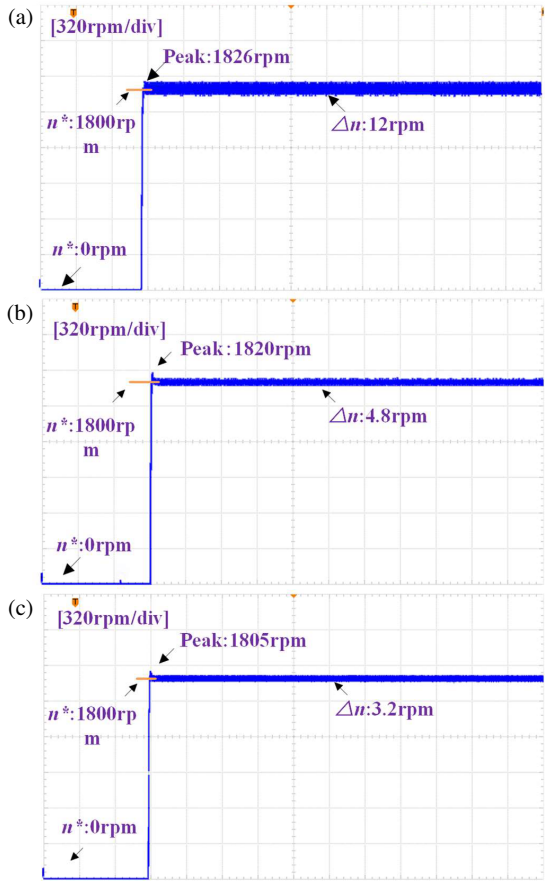

FIGURE 12. Speed variation under no-load startup. (a) MRAS, (b) STA-MRAS, (c) FASTA-FC-MRAS.

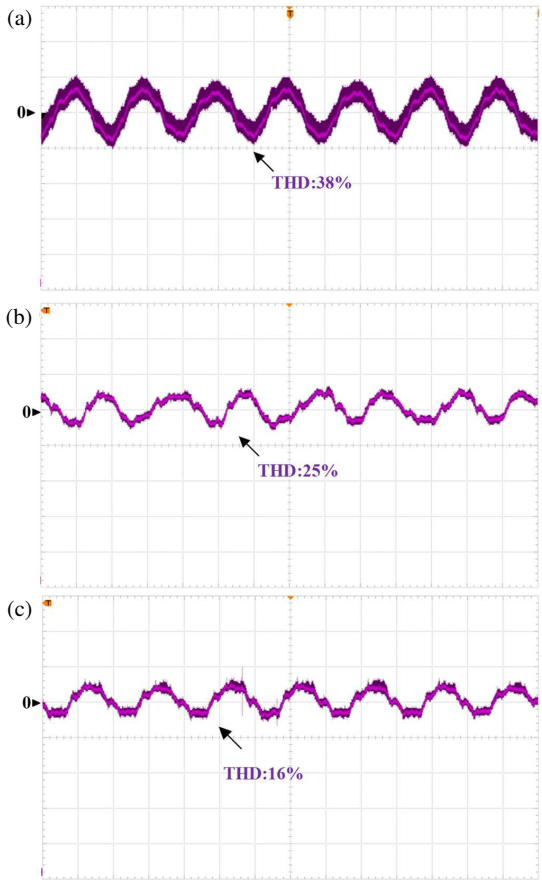

FIGURE 13. Phase A current of the motor during load increase. (a) MRAS, (b) STA-MRAS, (c) FASTA-STA-MRAS.

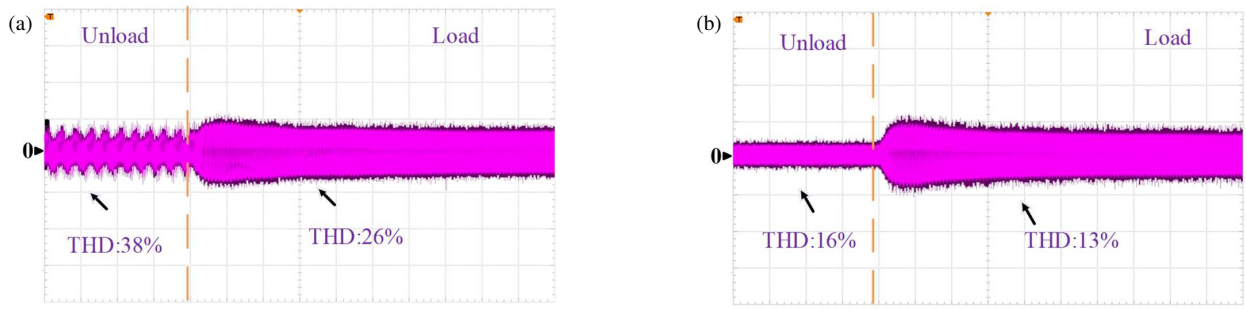

FIGURE 14. Phase A current of the motor during load increase. (a) FC-MRAS, (b) FASTA-FC-MRAS.

4.4. Dynamic Response Analysis

To compare the dynamic response speed of MRAS, STA-MRAS, and FASTA-FC-MRAS control algorithms, the motor starts at 1200 rpm and, after a period, accelerates to 1800 rpm. The time required to accelerate from 1200 rpm to 1800 rpm is analyzed, as shown in Figures 16(a), (b), and (c), respectively.

In Figure 16(a), MRAS exhibits a relatively fast current convergence speed when the speed increases, reaching a stable state after 0.5 seconds. In contrast, in Figure 16(b), the current convergence in STA-MRAS is slower, stabilizing after 0.3 seconds. Figure 16(c) shows that FASTA-FC-MRAS has the fastest convergence speed, completing the convergence in just 0.2 seconds.

The traditional PI adaptive mechanism has poor disturbance rejection capability, leading to slower convergence speeds when speed changes occur. As a result, MRAS has slower convergence. The conventional second-order sliding mode has a limited approaching speed to the sliding surface, which causes a slight delay in current convergence when STA-MRAS faces speed changes. In contrast, FASTA-FC-MRAS accelerates the approach to the sliding surface by introducing the fast super-twisting algorithm, thus improving the current convergence speed during speed changes.

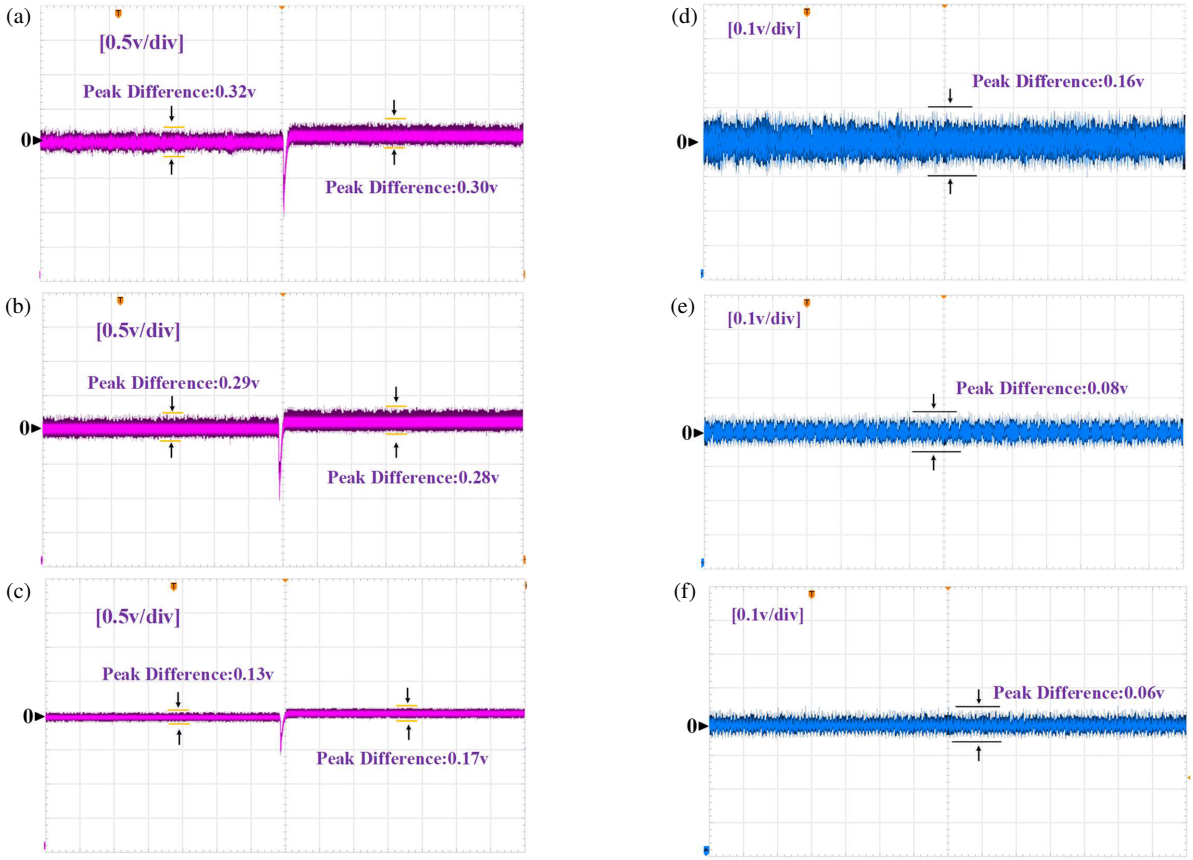

FIGURE 15. d-q axis voltage during speed increase. (a) MRAS (u_q), (b) STA-MRAS (u_q), (c) MRAS (u_q), (d) MRAS (u_d), (e) STA-MRAS (u_d), (f) STA-MRAS (u_d).

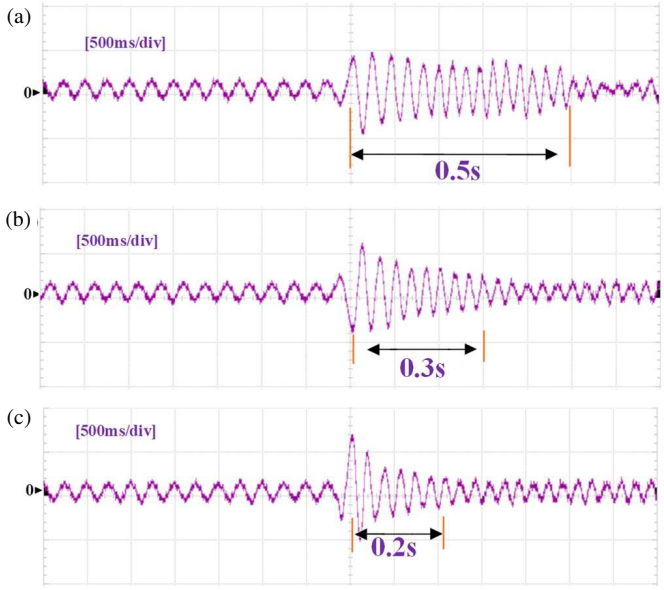

FIGURE 16. Comparison of current convergence speed under increasing rotational speed. (a) MRAS, (b) STA-MRAS, (c) FASTA-FC-MRAS.

4.5. Stability Analysis under Parameter Variation

In practical applications, the resistance of PMSM inevitably varies due to environmental temperature factors. These mismatches may lead to reduced accuracy in rotor position estimation, thereby degrading overall system performance. Therefore, this section selects stator resistance as the mismatched parameter for investigation. To meet the requirements of real-world applications, resistance mismatches of $R = 0.8R_s$ and $R = 1.2R_s$ are employed for validation.

Figure 17 demonstrates the experimental comparisons among MRAS, STA-MRAS, and FASTA-FC-MRAS under model mismatch conditions, where the stator resistance varies from R_s to $0.8R_s$ and $1.5R_s$ during motor speed transitions from 1200 rpm to 1800 rpm. As shown in Figure 17(a), under parameter mismatch conditions, the speed fluctuation of conventional MRAS increases from 15.7 rpm to 17.6 rpm, indicating significant variations in speed oscillation. This phenomenon stems from the inherent dependency of traditional MRAS on model parameters through its adjustable and reference model configuration. In Figure 17(b), STA-MRAS exhibits minor speed fluctuations ranging from 6.3 rpm to 6.5 rpm. Notably, FASTA-FC-MRAS demonstrates speed fluctuations between 6.4 rpm and 7.8 rpm when the resistance varies from $0.8R_s$ to $1.2R_s$. Compared with conventional MRAS, the proposed scheme shows substantial improvement in speed estimation performance under parameter mismatch conditions. However, a discernible gap remains in speed fluctuation suppression between the improved scheme and STA-MRAS under parameter mismatches, which provides clear optimization directions for subsequent research.

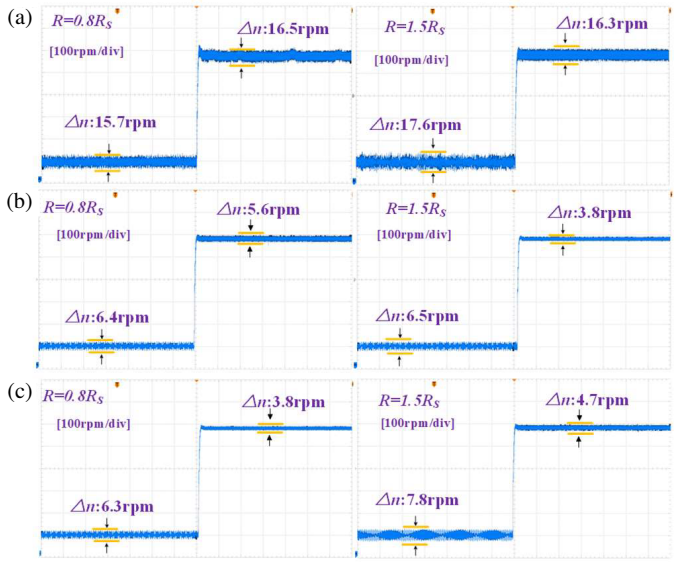

FIGURE 17. Comparison of speed chattering suppression ability under parameter variation. (a) MRAS, (b) STA-MRAS, (c) FASTA-FC-MRAS.

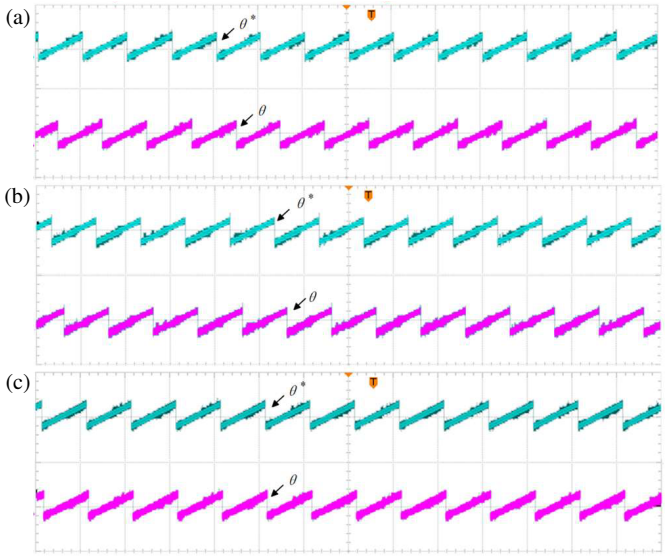

FIGURE 18. Comparison of rotor estimated position and actual position. (a) MRAS, (b) STA-MRAS, (c) FASTA-FC-MRAS.

4.6. Rotor Position Estimation Performance Analysis

With the motor maintaining a speed of 1800 rpm, the rotor estimated positions under three different control methods are compared. From Figures 18(a), (b), and (c), it can be seen that the rotor estimated positions of the traditional MRAS and STA-MRAS methods have a certain deviation from the actual position, while the rotor estimated position of the proposed FASTA-FC-MRAS control strategy has a smaller error and can reliably follow the actual rotor position.

5. CONCLUSION

This paper proposes a control method integrating the FASTA with the MRAS for sensorless control of PMSM. First, a feedforward compensation term is introduced into the conventional MRAS, and an adaptive rate for tracking speed variations is integrated to minimize speed errors and enhance decoupling between the adjustable and reference models. Additionally, a fast super-twisting sliding mode algorithm with an exponential acceleration term is proposed to replace the PI controller in MRAS, thereby improving the system convergence speed while guaranteeing stability. Experimental comparisons with MRAS, STA-MRAS, and FASTA-FC-MRAS demonstrate that the proposed method reduces rotational speed fluctuations by 76% and 45%, improves current convergence speed by 60% and 34%, and exhibits superior dynamic response compared to traditional MRAS and STA-MRAS. These findings hold significant reference value for practical engineering applications, and the strategy is expected to be applied in industrial automation and robotics.

Future research will focus on the following two aspects: 1) simplify the algorithmic model and reduce the amount of algorithmic computation, and 2) improve the performance of the observer to make it suitable for low-speed motors.

REFERENCES

[1] Yin, Y., L. Liu, S. Vazquez, R. Xu, Z. Dong, J. Liu, J. I. Leon, L. Wu, and L. G. Franquelo, "Disturbance and uncertainty attenuation for speed regulation of PMSM servo system using adaptive optimal control strategy," *IEEE Transactions on Transportation Electrification*, Vol. 9, No. 2, 3410–3420, Jun. 2023.

[2] Gao, J., C. Gong, W. Li, and J. Liu, "Novel compensation strategy for calculation delay of finite control set model predictive current control in PMSM," *IEEE Transactions on Industrial Electronics*, Vol. 67, No. 7, 5816–5819, Jul. 2020.

[3] Yin, Z., Y. Zhang, X. Cao, D. Yuan, and J. Liu, "Estimated position error suppression using novel PLL for IPMSM sensorless drives based on full-order SMO," *IEEE Transactions on Power Electronics*, Vol. 37, No. 4, 4463–4474, Apr. 2022.

[4] Gong, C., Y. Hu, J. Gao, Y. Wang, and L. Yan, "An improved delay-suppressed sliding-mode observer for sensorless vector-controlled PMSM," *IEEE Transactions on Industrial Electronics*, Vol. 67, No. 7, 5913–5923, Jul. 2020.

[5] Han, L., S. Wang, Z. Wang, X. Zhu, and W. Nie, "Design of compensated PLL for position sensorless drives of PMSMs," *Progress In Electromagnetics Research C*, Vol. 149, 25–35, 2024.

[6] Morawiec, M. and A. Lewicki, "Speed observer structure of induction machine based on sliding super-twisting and backstepping techniques," *IEEE Transactions on Industrial Informatics*, Vol. 17, No. 2, 1122–1131, Feb. 2021.

[7] Wang, G., D. Xiao, N. Zhao, X. Zhang, W. Wang, and D. Xu, "Low-frequency pulse voltage injection scheme-based sensorless control of IPMSM drives for audible noise reduction," *IEEE Transactions on Industrial Electronics*, Vol. 64, No. 11, 8415–8426, Nov. 2017.

[8] Han, B., Y. Shi, X. Song, K. Hong, and K. Mao, "Initial rotor position detection method of SPMSM based on new high frequency voltage injection method," *IEEE Transactions on Power Electronics*, Vol. 34, No. 4, 3553–3562, Apr. 2019.

[9] Liu, J. and Y. Zhang, "Performance improvement of nonlinear flux observer for sensorless control of PMSM," *IEEE Transac-*

tions on Industrial Electronics, Vol. 70, No. 12, 12 014–12 023, Dec. 2023.

[10] Hu, J., Z. Wang, H. Wang, and C. He, "Gain compensation-based quasi-resonant PLL with adaptive super-twisting SMO for position error suppression of IPMSM sensorless control," *IEEE Journal of Emerging and Selected Topics in Power Electronics*, Vol. 12, No. 5, 4888–4899, Oct. 2024.

[11] Xiao, L., J. Zhang, H. Xie, and C. Hu, "A novel speed estimation algorithm for a permanent magnet linear synchronous motor using an extended Kalman filter with multiple fading factors," *IEEE Transactions on Magnetics*, Vol. 60, No. 11, 1–5, Nov. 2024.

[12] Wang, F., Z. Chen, P. Stolze, J.-F. Stumper, J. Rodríguez, and R. Kennel, "Encoderless finite-state predictive torque control for induction machine with a compensated MRAS," *IEEE Transactions on Industrial Informatics*, Vol. 10, No. 2, 1097–1106, May 2014.

[13] Yu, J., P. Shi, W. Dong, B. Chen, and C. Lin, "Neural network-based adaptive dynamic surface control for permanent magnet synchronous motors," *IEEE Transactions on Neural Networks and Learning Systems*, Vol. 26, No. 3, 640–645, Mar. 2015.

[14] Azza, H. B., N. Zaidi, M. Jemli, and M. Boussak, "Development and experimental evaluation of a sensorless speed control of SPIM using adaptive sliding mode-MRAS strategy," *IEEE Journal of Emerging and Selected Topics in Power Electronics*, Vol. 2, No. 2, 319–328, Jun. 2014.

[15] Jiang, Y., D. Shi, J. Fan, T. Chai, and T. Chen, "Event-triggered model reference adaptive control for linear partially time-variant continuous-time systems with nonlinear parametric uncertainty," *IEEE Transactions on Automatic Control*, Vol. 68, No. 3, 1878–1885, Mar. 2023.

[16] Jiang, N., R. Cao, W. Sun, D. Chen, and K. Wang, "MRAS-based sensorless control of PMSM drives using extended state observer in shaftless rim-driven thruster system," *IEEE Transactions on Transportation Electrification*, Vol. 11, No. 2, 6038–6047, Apr. 2025.

[17] Yang, Y., X. Sun, and F. Cai, "Speed sensorless control of IPMSM with model predictive current control plus finite position set MRAS observer," *IEEE Transactions on Transportation Electrification*, Vol. 11, No. 1, 4755–4764, Feb. 2025.

[18] Wang, T., Y. Yu, Z. Zhang, S. Jin, B. Wang, and D. Xu, "An auxiliary variable-based MRAS speed observer for stable wide-speed operation in sensorless induction motor drives," *IEEE Journal of Emerging and Selected Topics in Power Electronics*, Vol. 12, No. 5, 4926–4940, Oct. 2024.

[19] Wang, H., X. Ge, and Y.-C. Liu, "Second-order sliding-mode MRAS observer-based sensorless vector control of linear induction motor drives for medium-low speed maglev applications," *IEEE Transactions on Industrial Electronics*, Vol. 65, No. 12, 9938–9952, Dec. 2018.

[20] Wang, T., B. Wang, Y. Yu, and D. Xu, "Discrete sliding-mode-based MRAS for speed-sensorless induction motor drives in the high-speed range," *IEEE Transactions on Power Electronics*, Vol. 38, No. 5, 5777–5790, May 2023.

[21] Chen, D., J. Wang, and L. Zhou, "Adaptive second-order active-flux observer for sensorless control of PMSMs with MRAS-based VSI nonlinearity compensation," *IEEE Journal of Emerging and Selected Topics in Power Electronics*, Vol. 11, No. 3, 3076–3086, Jun. 2023.

[22] Yuan, L., K. Han, C. Zhang, X. Zhu, and Y. Ding, "Comparative analysis of full-order SMO and STM-MRAS in SPMSM sensorless drive system," *IEEE Journal of Emerging and Selected Topics in Power Electronics*, Vol. 12, No. 3, 2592–2603, Jun. 2024.

[23] Moreno, J. A. and M. Osorio, "A Lyapunov approach to second-order sliding mode controllers and observers," in *2008 47th IEEE Conference on Decision and Control*, 2856–2861, Cancun, Mexico, Jan. 2008.

[24] Wang, D. and X. Liu, "Sensorless control of PMSM with improved adaptive super-twisting sliding mode observer and IST-QSG," *IEEE Transactions on Transportation Electrification*, Vol. 11, No. 1, 721–731, Feb. 2025.

[25] Ye, S. and X. Yao, "An enhanced SMO-based permanent-magnet synchronous machine sensorless drive scheme with current measurement error compensation," *IEEE Journal of Emerging and Selected Topics in Power Electronics*, Vol. 9, No. 4, 4407–4419, Aug. 2021.